A correlation-stability approach to elasticity mapping in optical coherence tomography

2013 Laser Phys. Lett. 10 065601

(http://iopscience.iop.org/1612-202X/10/6/065601)

Laser Phys. Lett. **10** (2013) 065601 (5pp) doi:10.1088/1612-2011/10/6/065601

LETTER

A correlation-stability approach to elasticity mapping in optical coherence tomography

V Yu Zaitsev[1,2], L A Matveev[1,2], G V Gelikonov[1], A L Matveyev[1] and V M Gelikonov[1,2]

[1] Institute of Applied Physics RAS, Uljanova Street 46, Nizhny Novgorod, Russia
[2] Nizhny Novgorod State University, Gagarina Avenue 23, Nizhny Novgorod, Russia

E-mail: vyuzai@hydro.appl-sci.nnov.ru

Received 30 January 2013, in final form 9 February 2013
Accepted for publication 11 February 2013
Published 22 April 2013
Online at stacks.iop.org/LPL/10/065601

Abstract
A variant of compressional optical coherence elastography for mapping of the relative stiffness of biological tissues is reported. Unlike conventionally discussed displacement-based (DB) elastography, in which the decrease in the cross-correlation between subsequently obtained images is a negative factor causing errors in the mapping displacement and strain fields, we propose to intentionally use the difference in the correlation stability (CS) for deformed-tissue regions with different stiffnesses. We compare the parameter ranges (in terms of noise-to-signal ratio and strain) in which the conventional DB and CS approaches are operable. It is shown that the CS approach has advantages such as a significantly wider operability region in terms of strain and is more tolerant to noise. This is favorable for freehand implementation of the CS approach. Examples of simulated and real CS-based elastographic optical coherence tomography images are given.

(Some figures may appear in colour only in the online journal)

1. Introduction

The problem of elasticity imaging in optical coherence tomography (OCT) has been attracting a great deal of attention since the end of the 1990s [1–11]. However, the elastography regime is not yet realized in commercial OCT scanners, whereas in medical ultrasonics combined conventional scans and shear-elasticity imaging are already implemented in several platforms (e.g., Siemens, Hitachi, Ultrasonix [12]). Although some ultrasonic systems use excitation of shear waves and measurement of their velocities (e.g., Fibroscan and Supersonic scanners) [12], elasticity imaging is mostly based on special processing of conventional ultrasonic images. Since the first work on OCT-elastography [1], similar processing of OCT images has often been discussed to reconstruct displacements produced by additional compression/shearing of the tissue. Subsequent differentiation of the displacement field can be used to determine the elastic-strain field and thus to estimate the shear-modulus distribution [1, 2].

Despite the apparent simplicity of the idea, the implementation of this approach faces significant difficulties and requires highly controllable laboratory conditions in experimental demonstrations (e.g. [1–3]). Indeed, numerical differentiation is rather error-sensitive and therefore requires accurate reconstruction of the displacement field. To fulfil this requirement, the deformations should not be too small. Otherwise, the pixelized structure of OCT images does not ensure acceptable accuracy even with the application of various super-resolution smoothing techniques [13, 12]. On

the other hand, the tissue strains should not be too large, because distortions of the scatterer patterns in the deformed OCT images reduce the accuracy of the cross-correlation (i.e., produce 'decorrelation noise' [13]). Other inevitable noise in real images introduces additional complications. In what follows we show that the above-mentioned factors limit the acceptable upper strain to several per cent. This limitation significantly complicates the realization of the most practically interesting freehand mode of elastography in OCT.

In what follows, we report an alternative variant of mapping of the relative stiffness using comparison of OCT images obtained under different degrees of straining. We call this variant the correlation-stability (CS) approach, bearing in mind that stiffer regions experience smaller distortions and demonstrate higher cross-correlation (which was also mentioned for ultrasonic scans [14]). After presenting numerical simulations and comparison with the conventional DB approach we give some *in vivo* examples of CS maps of relative elasticity distributions obtained in freehand mode using a spectral-domain OCT scanner.

2. The basic idea of the CS mapping and simulated examples

For the CS mapping, the reduction of cross-correlation between the images of the deformed tissue is an informative factor, rather than the 'decorrelation noise' reducing the mapping accuracy. There is a similarity with the nonlinear-acoustic approach to the detection of cracks (see, e.g., [15]), in which nonlinear distortions of the sounding field produced by increased nonlinearity of the defects are intentionally used as a signature of their presence. Basically, the procedure of cross-correlation between images using a moving (usually rectangular) window $m_1 \times m_2$ pixels in size is similar to that used in [1–3],

$$C(n,k) = \frac{\sum_i \sum_j (P_{i,j} - \mu_P)(R_{i+n,j+k} - \mu_R)}{\left[\sum_i \sum_j (P_{i,j} - \mu_P)^2 \sum_i \sum_j (R_{i+n,j+k} - \mu_R)^2\right]^{1/2}}, \quad (1)$$

where $i = 1 \ldots m_1, j = 1 \ldots m_2$, the window is moved by n pixels axially and k laterally, and $\mu_{P,R}$ are the mean values in $m_1 \times m_2$ areas on images P and R. For ideally coinciding areas $C(0,0) = 1$, and it tends to zero for uncorrelated ones. For real partially distorted and displaced areas, the position (n^*, k^*) is found where the correlation reaches maximum C^* and the field $C^*(i,j)$ is plotted as a CS map.

It should be emphasized that the proposed CS mapping should not be confused with the so-called correlation mapping method in OCT (cmOCT) intended to generate maps of microcirculation (see, e.g., [16, 17]). In the cmOCT approach, the studied region of the tissue is not deformed, and the subsequently obtained OCT images during the exposition period are directly cross-correlated (i.e. the window sliding is not performed). This corresponds to the condition that the parameters n and k describing the window motion in equation (1) are set to zero values. Under such conditions, the cross-correlation between the subsequent images remains equal to unity for non-moving parts of the tissue. In contrast, in the regions with the coordinates (i,j) corresponding to flows with moving scatterers, the correlation is reduced. This difference makes it possible to clearly distinguish such regions and efficiently map the microcirculation. As an indirect analogy, it can be said that the externally produced loading of the tissue causes the entire image to move. Although the trivial translational motion can be compensated by using the moving correlation window, the degree of mutual displacement of scatterers responsible for the cross-correlation decrease depends on the local stiffness. Just this fact is proposed to be used for elasticity mapping in the discussed CS approach.

To give an instructive example of the CS approach let us first consider a numerically simulated image of 400 × 200 pixels in size (typical of OCT images). The initial pattern of 'scatterers' is formed by putting a random value in each pixel. Then, Fourier filtering is applied to smooth the image and obtain a pattern of inhomogeneities with correlation properties similar to those typical of real OCT images. Namely, the filtering has to ensure that the simulated image has the same level of correlation between non-overlapped windows containing independent scatterers as in real OCT images. This background correlation C^{bg} is determined by the number $q_1 \times q_2$ of independent scatterers within the correlation window ($q_{1,2} \leq m_{1,2}$). It can be shown [18] that $C^{bg} = (\pi/2)^{1/2}/(q_1 q_2)^{1/2}$. In real OCT images, e.g., of human skin, typically $C^{bg} \sim 0.3$–0.2 for window sizes $m_{1,2} \sim$ 20–40 (similar windows were used in [2]). Such values of C^{bg} correspond to sizes of independent scatterers of about several pixels, which is ensured by the above-described procedure of generating the reference (initial) images.

The next step is to simulate how the created strain affects the images. In real experiments the surface of the OCT sensor acts as a rigid piston, producing strain fields combining axial and lateral components u_{ij}, where $u(x,y,z)$ is the displacement field. Here, for illustration we consider purely shear lateral deformation. This allows one to use a simple analytical solution even for inhomogeneous tissue containing a layer with a contrasting shear modulus $\mu_2 = b\mu$, where $\mu = \mu_1 = \mu_3$ is the modulus of the surrounding upper and lower layers, and b is the contrast. If the total sample thickness is $l = l_1 + l_2 + l_3$, where l_2 is the contrasting-layer thickness (see figure 1(a)) and the lateral displacement of the tissue surface is u_0, then the lateral displacements $u(z)$ inside the sample are

$$u(z) = \begin{cases} \dfrac{u_0}{A}\dfrac{z\mu_2}{\mu_1 l_2}, & 0 \leq z \leq l_1, \\ \dfrac{u_0}{A}\left[\dfrac{\mu_2 l_1}{\mu_1 l_2} + \dfrac{z - l_1}{l_2}\right], & l_1 \leq z \leq l_2, \\ \dfrac{u_0}{A}\left[\dfrac{\mu_2 l_1}{\mu_1 l_2} + 1 + \dfrac{(z - l_1 - l_2)\mu_2}{\mu_3 l_2}\right], & l_2 \leq z \leq l_3, \end{cases} \quad (2)$$

where $A = 1 + \frac{\mu_2 l_1}{\mu_1 l_2} + \frac{\mu_2 l_3}{\mu_3 l_2}$ and the mean shear strain is $\varepsilon = u_0/l$. The patterns of the scatterers in the sheared sample can be recalculated using equations (2). Continuous subpixel displacements can also be correctly found using equations (2)

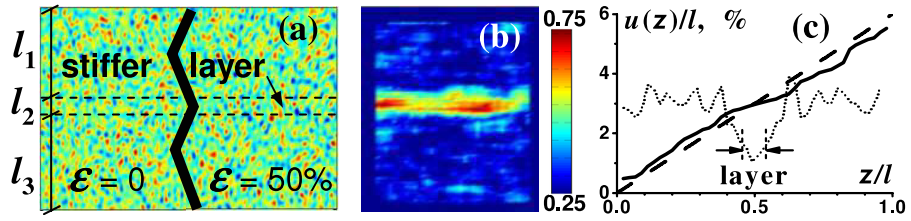

Figure 1. Simulated example of mapping of the stiffer layer with contrast $b = 3$ and thickness $l_2 = 20$ pixels. (a) The pattern of scatterers with $C^{bg} \approx 0.3$ for $\varepsilon = 0\%$ and $\varepsilon = 50\%$; (b) the CS image of the stiffer layer obtained by cross-correlating the unstrained pattern with the deformed one (see (a)); (c) the mean displacement $u_m(z)$ (dashed line), reconstructed lateral displacement $u(z)$ (solid line) along one of the vertical paths and its derivative averaged over all such cuts (dotted line) found by the conventional cross-correlation technique for a mean shear strain of 6%. The correlation-window size is 20 × 20 pixels. The images contain no additional noise and the errors are exclusively due to deformation of the scatterer pattern.

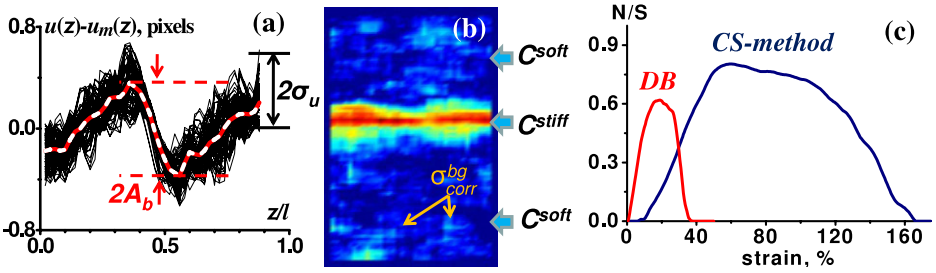

Figure 2. Elucidation of the determination of the operability areas for the conventional DB and CS mapping. (a) A bunch of vertical slices for $u(z) - u_m(z)$ with the mean 'butterfly' of amplitude A_b corresponding to the stiffer layer and irregularities in the reconstructed displacements with variance σ_u; (b) the CS map with regions having a difference in the mean correlation $\langle C^{stiff} - C^{soft} \rangle$ and a background variance σ^{bg}_{corr}; (c) the operability regions of the two methods in terms of strain and noise-to-signal ratio N/S defined as the ratio of square roots of the noise and signal energies (found after subtraction of the respective mean values).

and applying forward and inverse Fourier transforms of the pattern in combination with the theorem about the Fourier spectrum of shifted functions.

Figure 1(a) shows the initial and deformed patterns of simulated scatterers in which the contrasting-stiffness layer is not yet visible. An example of CS mapping of this layer is shown in figure 1(b), where the stiffer layer is clearly seen due to the increased correlation compared with the surrounding softer layers that experience stronger distortions. Finally, figure 1(c) shows the reconstructed displacements in a vertical slice using the conventional cross-correlation approach (with parabolic smoothing of the correlation peaks to obtain subpixel resolution).

In figure 1(c) the stiffer layer looks like a butterfly-like deviation of the $u(z)$ function (solid line) from the dashed line $u_m(z)$ corresponding to the mean shear of the entire sample. Conventionally [1], the so-found displacement field is supposed to be differentiated to obtain the strain field (the dotted line shown in figure 1(c) in arbitrary units). The regions with smaller local strains correspond to larger stiffness.

The procedure of numerical differentiation of the reconstructed displacement field is known to introduce additional errors in the resulting strain field (even if there is no other noise than the deformation-produced 'decorrelation noise' [13]). For instance, in figure 1(c) the dotted line corresponding to differentiation of the reconstructed displacements over the vertical coordinate is averaged over all vertical sections of the image. However, even after such averaging the reconstructed strain demonstrates pronounced irregularities. The irregularities in figure 1(c) are solely due to the 'decorrelation noise' in terms of the paper [13], i.e., strain-produced distortions of the scatterer pattern. Hereafter, all other distortions of the image unrelated to the stress-produced deformation of the scatterer pattern we call 'noise'.

3. Comparison of operability regions for the CS mapping and DB mapping in terms of tissue strain and noise-to-signal ratio

Now we compare the operability regions for the proposed CS mapping and conventional DB elasticity mapping in terms of strain and tolerance to additional noise. In our comparison we even adopt the form more favorable for the conventional DB approach. Namely, we will not apply the procedure of error-sensitive differentiation taking into account that the displacement field itself can already allow one to detect the presence of stiffer regions (this is also mentioned in [1]).

In what follows, we will directly use the presence of the 'butterfly' shown in figure 1(c) as a signature of the presence of the stiffer layer. For better clarity, the mean slope of the displacement distribution (see the dashed line in figure 1(c)) can be subtracted to obtain a horizontally-oriented 'butterfly' in the region of the stiffer layer, as shown in figure 2(a). The informative 'butterfly' with amplitude A_b can be masked by various irregularities characterized by the variance σ_u due to the presence of noise and decorrelation distortions of the scatterer pattern in OCT images. As the

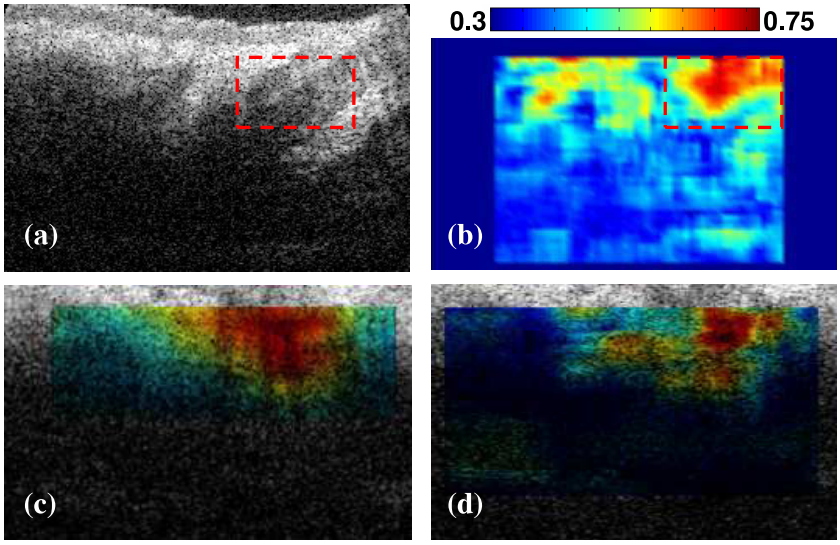

Figure 3. Two *in vivo* examples of CS maps of relative stiffness where the red color shows the stiffer regions. Panel (a) shows a conventional OCT image where a hair root is hardly seen and (b) is the corresponding CS map for a correlation-window size of 20×20 pixels. Panels (c) and (d) show OCT images of another bulb superposed with the elastographic CS maps with different resolution obtained using windows of 40×40 and 20×20 pixels, respectively.

threshold condition we adopt the 'three-sigma criterion' often used in statistics, i.e., $A_\mathrm{b} \geq 3\sigma_u$. The variance σ_u of the irregularities is estimated for each given strain by gradually increasing the amplitude of the generated additional noise and then comparing σ_u with A_b. For the CS mapping, we make a similar comparison between the cross-correlation level C^stiff for the stiffer layer and C^soft for the surrounding softer areas. These two levels of cross-correlation are characterized by their respective average values and the background cross-correlation variance $\sigma^\mathrm{bg}_\mathrm{corr}$ (which is due to irregularities in the cross-correlation coefficient that are always present even in the absence of the stiffer layer). For a given strain, we vary the noise level and again determine the threshold difference $\langle C^\mathrm{stiff} - C^\mathrm{soft} \rangle = 3\sigma^\mathrm{bg}_\mathrm{corr}$. The so-found curves delimiting the operability regions for the DB and CS mapping are shown in figure 2(c). We emphasize that in figure 2(c) the vertical axis is for noise-to-signal ratio (i.e. the inverse value of the more conventional signal-to-noise ratio), so that points more distant from the coordinate system origin correspond to stronger noise and larger strains. In agreement with other authors [13, 4] we found that the conventional DB mapping works for fairly small (below ~10%) strains, whereas the CS mapping works in a much wider range of larger strains (~20–150%), which is favorable for freehand operation. Besides, CS mapping is noticeably more tolerant to noise.

4. Examples of elastographic CS maps obtained for real OCT images

For the demonstrations, we used a recently developed OCT spectral-domain scanner based on techniques described in [19, 20]. It acquires 480×289 pixel images with a rate of 21 fps, axial resolution of 10 μm and lateral resolution of 20 μm. The fiber-optic OCT probe with a 'forward-looking' window 2 mm in diameter has a built-in scanning system ensuring obtaining of B-scans. The probe acts as a piston producing deformation of the tissue during freehand operation. The series of obtained OCT images of the tissue deformed by the varied probe pressure is fed into a PC in real time. After filtering, amplitude normalization, and averaging of a few frames, the images are cross-correlated with a reference one to produce CS maps.

For *in vivo* examples of CS mapping we chose human cheek skin, where the hair roots play the role of stiffer inclusions. Examples of thus-obtained CS maps are shown in figure 3, where the stiffer regions are clearly seen. For these examples, the average strain created in the tissue by pressing the probe onto the skin is about 20–50%, in agreement with the above-found operability region for CS mapping.

To avoid eventual misinterpretation, it can be emphasized that the difference in the cross-correlation level between different parts of the obtained maps should not be directly interpreted as the ratio of the stiffness properties, because the relation of the latter to the decorrelation, generally speaking, is a nonlinear function. Therefore, the thus-obtained CS maps give a relative and qualitative representation of the stiffness inhomogeneity similar to the result of tissue palpation (although certainly no direct palpation is possible at the OCT scale). However, even such relative characterization of the tissue stiffness can already be useful in the same sense as results of macroscopic palpation.

It can be added that in the presented examples, the speckling of the deformed-tissue images is significantly reduced by applying averaging and filtering, so that the remaining pattern is mostly determined by morphological inhomogeneities of the tissue. However, for deformed tissues, the decorrelation rate due to speckling is also essentially determined by the local stiffness, because relative displacements of sub-resolved scatterers are smaller in stiffer regions just as for visible morphological features. Thus,

generally speaking, the correlation-stability principle can be extended to the level of individual speckling pixels. Although special analysis is needed for such a regime, evidently its operability region should be shifted to smaller strains to ensure sufficient similarity of the correlated images.

5. Discussion of the CS elasticity mapping in the context of alternative methods

In the historically formed terminology, the proposed CS approach can be viewed as a kind of 'compressional' elastography [12] by analogy with other elastographic methods based on creation of additional quasi-static deformation of the tissue. However, it should be clearly understood that the probe-produced strains of the order of tens of per cent have nothing to do with a genuine hydrostatic compression of the same magnitude. Indeed, since for soft biological tissues the Poisson's coefficient is very close to 0.5 (like for liquids), the strain-tensor spur $\sum_i u_{ii}$ (the volumetric tissue strain) in the vicinity of the pressing probe remains nearly zero, even though the individual strain components u_{ij} responsible for decorrelation of the scatterer patterns may reach tens of per cent. For CS mapping, it is not particularly important which of the strain-tensor components cause the scatterer-pattern distortion and decorrelation of the compared images. Figure 2(c) illustrates that implementation of CS mapping requires noticeably higher strains than the DB approach. This difference follows from the very principle of CS mapping: the distorted images should be sufficiently decorrelated (down to the above-discussed background level over the most part of the frame), whereas the conventional DB approach, in contrast, implies small distortions to ensure sufficient correlation between the images for fairly accurate reconstruction of the displacement and strain fields.

However, straightforward increase only in the sensitivity of displacement detection is not sufficient to ensure high-quality reconstruction of strains in the DB approach. Indeed, taking, for instance, the one-dimensional distribution of displacements $u(z)$, it is clear that the quality of differentiation $\mathrm{d}u/\mathrm{d}z \approx (u_2 - u_1)/(z_2 - z_1)$ is determined not only by the displacement sensitivity responsible for the accuracy of $u_{1,2}$ measurement, but also by the measurement resolution responsible for the absolute accuracy of determining the positions $z_{1,2}$ of the scatterers. Thus, although the displacement sensitivity can be rather high, for example, in phase-sensitive measurements [9, 10], the main limiting factor for high-quality reconstruction of strain is the measurement resolution (which also determines the pixelized structure of the images). Simple use of averaged strain, $u(z)/z$, like in [9, 10] instead of differentiation, $\mathrm{d}u/\mathrm{d}z$, still does not yield the genuine local strain distribution, although more sophisticated methods can be used to improve the estimation of local strains [21]. Besides, for the most practically interesting freehand mode of OCT probe operation, the feasibility of such sophisticated high-accuracy strain estimations can be problematic (influence of hand tremor, not only axial motion of scatterers, etc).

The proposed rather straightforward CS approach looks like an attractive simple alternative for obtaining qualitative elastographic maps. The performed analysis and tests demonstrate that it can be readily implemented in sufficiently high-speed OCT scanners in freehand mode to obtain relative-stiffness maps similar to those used in medical ultrasonics [12].

Acknowledgments

The authors acknowledge the support of the Russian Foundation for Basic research and grant 11.G34.31.0066 of the Russian Federation Government. L A Matveev acknowledges the support of grant No. MK-4826.2013.2 of the President of the Russian Federation.

References

[1] Schmitt J 1998 *Opt. Express* **3** 199
[2] Rogowska J, Patel N A, Fujimoto J G and Brezinski M E 2004 *Heart* **90** 556
[3] Rogowska J, Patel N, Plummer S and Brezinski M E 2006 *Br. J. Radiol.* **79** 707
[4] Kirkpatrick S S J, Wang R K and Duncan D D 2006 *Opt. Express* **14** 11585
[5] Bossy E, Funke A, Daoudi K, Boccara A-C, Tanter M and Fink M 2007 *Appl. Phys. Lett.* **90** 174111
[6] Adie S G, Liang X, Kennedy B F, John R, Sampson D D and Boppart S A 2010 *Opt. Express* **18** 25519
[7] Kennedy B F, Liang X, Adie S G, Gerstmann D K, Quirk B C, Boppart S A and Sampson D D 2011 *Opt. Express* **19** 6623
[8] Sun C, Standish B and Yang V X D 2011 *J. Biomed. Opt.* **16** 043001
[9] Wang R K, Ma Z H and Kirkpatrick S J 2006 *Appl. Phys. Lett.* **89** 144103
[10] Wang R K, Kirkpatrick S and Hinds M 2007 *Appl. Phys. Lett.* **90** 164105
[11] Kennedy B F, Curatolo A, Hillman T R, Saunders C M and Sampson D D 2011 *J. Biomed. Opt.* **16** 020506
[12] Parker K J, Doyley M M and Rubens D J 2011 *Phys. Med. Biol.* **56** R1
[13] Ophir J, Alam S, Garra B, Kallel F, Konofagou E E, Krouskop T, Merritt C R B, Souchon R, Spinivasan S and Varghese T 2002 *J. Med. Ultrason.* **29** 155
[14] Shao J, Bai J, Cui L, Wang J, Fu Y, Liu K and Feng S 2007 *J. Ultrasound Med.* **26** 1191
[15] Zaitsev V Y, Nazarov V E and Talanov V I 2006 *Phys.—Usp.* **49** 89
[16] Enfield J, Jonathan E and Leahy M 2011 *Biomed. Opt. Express* **2** 1184–93
[17] Jonathan E, Enfield J and Leahy M J 2011 *J. Biophoton.* **4** 583–7
[18] Bendat J S and Piersol A G 1986 *Random Data: Analysis and Measurement Procedures* (New York: Wiley)
[19] Gelikonov V M, Gelikonov G V and Shilyagin P A 2009 *Opt. Spectrosc.* **106** 459
[20] Gelikonov V M, Gelikonov G V, Kasatkina I V, Terpelov D A and Shilyagin P A 2009 *Opt. Spectrosc.* **106** 895
[21] Kennedy B F, Koh S H, McLaughlin R A, Kennedy K M, Munro P R T and Sampson D D 2012 *Biomed. Opt. Express* **3** 1865